



1 Comparisons and quality control of wind observations 2 in a mountainous city using wind profile radar and the 3 Aeolus satellite

4 Hua Lu^{1, 3}, Min Xie^{1, 2}, Wei Zhao⁴, Bojun Liu⁵, Tijian Wang¹, Bingliang Zhuang¹

5 ¹School of Atmospheric Sciences, Nanjing University, Nanjing 210023, China

6 ²School of Environment, Nanjing Normal University, Nanjing 210023, China

7 ³Chongqing Institute of Meteorological Sciences, Chongqing 401147, China

8 ⁴Nanjing Institute of Environmental Sciences, Ministry of Ecology and Environment of the People's
9 Republic of China, Nanjing 210023, China

10 ⁵Chongqing Meteorological Observatory, Chongqing 401147, China

11 *Correspondence to:* Min Xie (minxie@nju.edu.cn), Wei Zhao (zhaowei@nies.org)

12 **Abstract:** Observations of vertical wind in Chongqing, a typical mountainous city in China, are
13 important, but sparse and have low resolution. To obtain more wind profile data, this study matched
14 the Aeolus track with ground-based wind observation sites in Chongqing in 2021. Based on the
15 obtained results, verification and quality control studies were conducted on the wind observations of a
16 wind profile radar (WPR) with radiosonde (RS) data, and a comparison of the Aeolus Mie-cloudy and
17 Rayleigh-clear wind products with WPR data was then performed. The conclusions can be
18 summarized as follows: (1) A clear correlation between the wind observations of WPR and RS was
19 found, with a correlation coefficient (R) of 69.92%. Their root-mean-square deviation increased with
20 height but decreased by 3–4 km. (2) After quality control of Gaussian filtering (GF) and empirical
21 orthogonal function construction (EOFc, $G = 87.23\%$) of the WPR data, the R between the WPR and
22 RS reached 76.00% and 95.44%, respectively. The vertical distribution showed that GF could better
23 retain the characteristics of WPR wind observations, but with limited improvement in decreasing
24 deviations, whereas EOFc performed better in decreasing deviations, but considerably modified the
25 original characteristics of the wind field, especially regarding intensive vertical wind shear in strong
26 convective weather processes. (3) In terms of the differences between the Aeolus and WPR data,
27 56.0% and 67.8% deviations were observed between ± 5 m/s for Rayleigh-clear and Mie-cloudy
28 winds vs. WPR winds, respectively. Vertically, the mean differences of both Rayleigh-clear and
29 Mie-cloudy winds versus WPR winds appeared below 1.5 km, which is attributed to the prevailing
30 quiet and small winds within the boundary layer in Chongqing, such that the movement of molecules
31 and aerosols is mostly affected by irregular turbulence. Additionally, large mean differences of 4–8



32 km for Mie-cloudy versus WPR winds may be related to the high content of cloud liquid water in the
33 middle troposphere, influenced by the topography of the Tibetan Plateau. (4) The differences in both
34 Rayleigh-clear and Mie-cloudy versus WPR winds had changed. Deviations of 58.9% and 59.6%
35 were concentrated between ± 5 m/s for Rayleigh-clear versus WPR winds with GF and EOFc quality
36 control, respectively. In contrast, 69.1% and 70.2% of deviations appeared between ± 5 m/s for
37 Rayleigh-clear versus WPR and EOFc WPR winds, respectively. These results shed light on the
38 comprehensive applications of multi-source wind profile data in mountainous cities or areas with
39 sparse ground-based wind observations.

40 **Keywords:** Wind profile radar, Aeolus satellite, data verification, data quality control, mountainous
41 city

42 1 Introduction

43 The detection of the atmospheric wind profile is essential to study atmospheric dynamics,
44 interactions between weather and pollution, and predict extreme weather (Baker et al., 1995; King et
45 al., 2017; Stettner et al., 2019; Sun et al., 2022). Furthermore, the value of atmospheric wind
46 observations has been illustrated by assimilation applications in numerical weather prediction
47 (Benjamin et al., 2004; Weissmann et al., 2007; Michelson and Bao, 2008). In particular, wind fields
48 within the boundary layer are mostly turbulent and difficult to simulate using models without the
49 assimilation of wind observations (Belmonte and Stoffelen 2019; Simonin et al., 2014). For areas
50 with complex terrain, such as mountainous cities, individual ground-based observation stations
51 usually have poor representation, and thus vertical observations are essential (Sekula et al., 2021; Lu
52 et al., 2022b). Therefore, unconventional wind profile observations are urgently required for analysis
53 and assimilation into numerical prediction models to describe the transport of mesoscale weather
54 systems, as well as to advance our knowledge of atmospheric component movement in the actual
55 atmosphere.

56 Wind profile radar (WPR) data may partially compensate for the limitations of conventional
57 wind field observations. WPR detects the scattering effect of atmospheric turbulence on
58 electromagnetic waves to detect the Doppler effect signals of air movement, and is capable of
59 providing horizontal wind vectors with high temporal and vertical resolution (Weber et al., 1990;
60 Dibbern et al., 2001). The automated, continuous, and real-time vertical wind profiles from the WPR



61 could fill the gaps in upper-air observations, both in time continuity and vertical resolution. Terrain
62 and climate characteristics in unique regions could have different impacts on WPR echoes, resulting
63 in separate data observation errors. Therefore, data verification, and occasionally adequate quality
64 control, are required before the application of WPR data in a specific region (Zhang et al., 2017; Guo
65 et al., 2020). In comparison, radiosonde (RS) data are often considered reliable atmospheric wind
66 observations to verify WPR data (Weber et al., 1990; Chen et al., 2022).

67 Owing to advances in satellite detection, wind fields acquired from satellites can supplement
68 conventional ground-based observations in space coverage. Atmospheric motion vector detection can
69 only extract the wind information of layers with clouds. The United States and Europe have
70 successively detected sea surface wind fields using microwave radiometers and scatterometers
71 (Endlich et al., 1971; Njoku et al., 1980; Gaiser et al., 2004; Barre et al., 2008). The World
72 Meteorological Organization regards the detection of global three-dimensional wind fields as one of
73 the most challenging and important meteorological observation missions in the 21st century (WMO,
74 2001). The United States and Europe have conducted space-borne wind lidar measurement programs,
75 as these are the best methods for detecting three-dimensional wind fields (Beranek et al., 1989; Baker
76 et al., 2008; Wernham et al., 2016). The Aeolus satellite was launched following the European Space
77 Agency's (ESA) fifth Earth Explorer mission on August 22, 2018. As the world's first Doppler wind
78 lidar in space, Aeolus has enabled the continuous detection of global wind profiles from the ground to
79 the lower stratosphere with a vertical resolution of 0.25–1 km (Marseille and Stoffelen, 2003;
80 Reitebuch et al., 2006; Zhang et al., 2019). Therefore, the wind profile data detected by Aeolus can
81 compensate for the lack of spatial coverage and vertical resolution of ground-based wind field
82 observations to some extent.

83 Located at the edge of the Sichuan Basin, Chongqing is a typical mountainous city in China
84 known for its complex topography and three-dimensional spatial structure. Owing to the unique
85 terrain, extreme weather forecasts and determining the movement of atmospheric components in the
86 city are complicated, making vertical observations essential. Interference sources for the vertical
87 detection of WPR might form in mountainous areas, which are different from those in plain areas.
88 Thus, reasonable data verification and quality control should be conducted before application to
89 ensure the accuracy and representativeness of the WPR. The spatial distribution of ground-based
90 vertical wind observations in Chongqing is sparse, and it is worthwhile to verify the performance of



91 Aeolus wind products and apply them to related mechanistic studies or numerical assimilation
92 systems. To this end, wind profile observations of RS, WPR, and Aeolus were collected and matched
93 in terms of time and space for 2021 in Chongqing. Based on the matched results, data verification and
94 quality control of WPR wind observations were implemented using RS data, and the performance of
95 Aeolus wind products in Chongqing was analyzed to provide a scientific basis for multi-source wind
96 profile data applications in mountainous cities. The remainder of this paper is organized as follows:
97 the RS, WPR, and Aeolus data used in this study, the matching procedure, data verification, and
98 quality control methods are described in Section 2; Section 3 presents the comparison and quality
99 control results of the WPR and Aeolus wind profile data; finally, the main conclusions are
100 summarized in Section 4.

101 **2 Data and methods**

102 **2.1 Data**

103 **2.1.1 Radiosonde wind data**

104 Station Shapingba (57516; 106.27°E, 29.34°N) is a national weather station and the only RS
105 station in Chongqing. Wind speed and direction at 0000 and 1200 UTC (universal time coordinated)
106 were obtained from an L-band sounding system on vertical height levels every 1 s from the surface to
107 30 km in the air (Zhang et al., 2020). RS wind data are generally reliable vertical observations and the
108 Shapingba WPR is located at the same station as RS; therefore, the data verification of WPR wind
109 observations was conducted based on RS data in this study.

110 **2.1.2 Wind profile radar data**

111 There are two wind profile radars in Chongqing, one at Shapingba station and the other at
112 Youyang station (57633; 108.46 ° E, 8.49 ° N). Radar can operate almost automatically and
113 continuously, acquiring vertical profiles of horizontal wind speed and wind direction (Guo et al.,
114 2021). The temporal and spatial vertical resolutions of the Shapingba and Youyang wind profile
115 radars were 5 min and 120 m, vertically detecting 48 and 45 layers up to 9360 and 8910 m,
116 respectively.

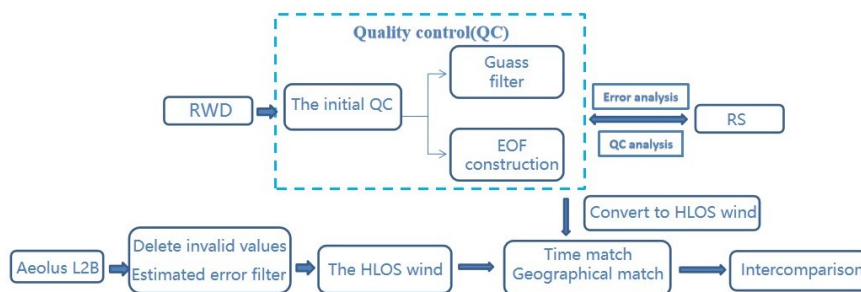


117 2.1.3 Aeolus wind products

118 Launched on August 22, 2018, the first space-borne Doppler wind lidar, Aeolus, developed by
119 the ESA, has been circling in a sun-synchronous orbit at an altitude of approximately 320 km, with a
120 7-day repeat cycle (ESA, 2008). Based on the original detection information, a series of products was
121 released by the ESA. The Aeolus Level-2B products can provide scientific wind products, which can
122 be used to obtain wind profile data from the ground to approximately 30 km in the air, with a vertical
123 resolution of 0.25–2 km and an uncertainty of 2–4 m/s, varying with height (Rennie et al., 2018; Chen
124 et al., 2022). Level-2B wind products are classified into Rayleigh-clear and Mie-cloudy winds.
125 Specifically, Rayleigh channels mainly detect wind fields with atmospheric molecules as tracers in
126 the troposphere and lower stratosphere, whereas the Mie channel detects signals from aerosols and
127 cloud droplet particles within the boundary layer or in the cloud (Witschas et al., 2020). In this study,
128 the horizontal line-of-sight (HLOS) wind products of both Rayleigh and Mie channels were used.
129 Additionally, the validity flag and estimated errors were extracted for quality control of HLOS wind
130 products (Tan et al., 2017; Guo et al., 2021).

131 2.2 Methods

132 2.2.1 Data matching and verification procedures



133 **Figure 1: Flowchart of the multi-source wind profile data matching and verification procedures.**

134 In an attempt to make full use of the multi-source vertical wind data from Chongqing,
135 appropriate procedures were used to match the RS, WPR, and Aeolus data in time and space
136 considering the limited ground-based wind profile observations. A flowchart of the procedure is
137 shown in Figure 1.



138 First, data verification and quality control effect analysis of the Shapingba WPR were
139 implemented based on RS data. Based on the approach used by Zhang et al. (2016) and Guo et al.
140 (2021), the Aeolus data were removed once the distances between adjacent tracks of Aeolus and
141 ground-based sites exceeded 1° . With this procedure, Shapingba station is not suitable for comparison
142 with Aeolus data, whereas Youyang WPR data is. Time and space matches of the WPR and Aeolus
143 data were posed before the comparison. Specifically, because of the higher temporal resolution of
144 WPR, the mean values of WPR data within 10 min before and after Aeolus sampling were used.
145 Vertically, Aeolus data were interpolated and matched to the layers of WPR data. Subsequently,
146 Aeolus data were screened by validity flags and estimated errors. Thereafter, both the original
147 Youyang WPR detection and quality control data were converted into HLOS winds for comparison
148 with the Aeolus data. The WPR wind vector was projected onto the HLOS winds using the following
149 equation (Witschas et al., 2020):

$$v_{RWP_{HLOS}} = \cos(\psi_{Aeolus} - wd_{RWP}) \cdot ws_{RWP}$$

150 Where ψ_{Aeolus} is the Aeolus azimuth angle, which could be extracted from the Level 2B products,
151 while wd_{RWP} and ws_{RWP} are WPR wind direction and speed, respectively.

152 2.2.2 Statistical method

153 The mean bias (MB) and root mean squared error (RMSE) were adopted as indicators (Equations
154 2 and 3) for the verification of the WPR and Aeolus wind products, which compares absolute and
155 relative deviations, respectively.

$$MB = \frac{1}{n} \sum_{i=1}^n (o(i) - r(i))$$
$$RMSE = \sqrt{\frac{\sum_{i=1}^n (o(i) - r(i))^2}{n}}$$

156 Where $o(i)$ represents the observation values and $r(i)$ represents the referent values.

157 2.2.3 Data quality control of the wind profile radar

158 2.2.3.1 The initial quality control

159 The first step in quality control is to eliminate the abnormal increase of horizontal wind in a
160 small vertical range of WPR data, including screening invalid data exceeding the climate extreme



161 values and the vertical consistency test. The extreme climate wind values on the relative layers are
162 listed in Table 1. For the vertical consistency test, if the wind difference between a specific layer and
163 its adjacent layer is greater than three times that of the two layers below, the value is considered as an
164 abnormal observation to be deleted (Zhang et al., 2015).

165 **Table 1: Extreme climate wind values in vertical layers**

Pressure(hPa)	1000	850	700	500	400	300	250
Height(m)	0	1500	3000	5500	7000	9000	10000
Extreme wind(m/s)	36.01	46.30	61.73	102.89	128.61	154.33	154.33

166 2.2.3.2 Gaussian filtering (GF) method

167 GF is a smooth filtering method that can be used to smooth out the details and noise of
168 two-dimensional graphs, and the observed value of the central point and its surrounding values are
169 summed in one-to-one correspondences. GF is similar to mean filtering, but its preset convolution
170 operator presents a Gaussian distribution. In this study, the convolutional operator was used to
171 calculate the weighted average of the WPR data to filter the high-frequency noise in the observation
172 of WPR. The Gaussian filtering function of the one-dimensional zero-mean normalization is as
173 follows:

$$g(x) = \frac{1}{\sqrt{2\pi}\sigma} e^{-\frac{x^2}{2\sigma^2}}$$

174 Where σ is the scale factor that determines the width of the Gaussian filter and further affects
175 the degree of data smoothing. The larger the σ value, the wider the frequency band of the Gaussian
176 filter, and the better the data smoothing effect. However, an excessively large σ value causes
177 excessive data loss and distortion. In this study, σ was set to 3.

178 2.2.3.3 Empirical orthogonal function construction (EOF) method

179 Based on the spatial-temporal sequence formed by wind field data W , calculations similar to
180 empirical orthogonal decomposition were performed, and the main modes obtained by calculation
181 were used to reconstruct the spatial-temporal sequence to construct new wind fields. Specifically, the
182 X matrix is formed by selecting N times, a period of time before and after a certain moment, and L
183 layers of effective data, vertically. X is represented below:



$$X = \begin{bmatrix} W_{1,1} & W_{1,2} & \cdots & W_{1,N} \\ W_{2,1} & W_{2,2} & & W_{2,1} \\ \vdots & \vdots & \ddots & \vdots \\ W_{L,1} & W_{L,2} & \cdots & W_{L,N} \end{bmatrix}$$

184 Subsequently, the covariance matrix of X, that is, $S = XX^T$, and its eigenvalues and eigenvectors
185 were calculated. According to the arrangement of the eigenvalues from largest to smallest, the
186 cumulative interpretation variance of the first m eigenvectors can be expressed as follows:

$$G = \left(\sum_{k=1}^m \lambda_k \right) / \left(\sum_{k=1}^L \lambda_k \right)$$

187 The larger the eigenvalue corresponding to the eigenvector, the more its corresponding
188 distribution reflects the typical characteristics of the original field. The time coefficient $T = ETX$ was
189 calculated with the eigenvector E. Finally, the main modes decomposed by EOF were used to
190 reconstruct the time series within N times, following the use of $X = ET$ to obtain the vertical
191 distribution of the wind field at the corresponding time. In the reconstruction of the time series, a
192 cut-off threshold ($G \geq 85\%$) was set for the interpretation of the cumulative variance to control the
193 quality of the observed data.

194 Assuming that the cumulative interpretation variances of the first m feature vectors met $G \geq 85\%$,
195 and the first m-1 did not meet $G \geq 85\%$, the feature vectors of the first m modes were adopted in the
196 reconstruction of the sequence, and the corresponding winds at moment j of the ith altitude layer are:

$$WS_{i,j} = \sum_{k=1}^m e_{i,k} t_{k,j}$$

197 The EOFc method can eliminate outliers and pulsating noise from observation data, and has been
198 applied in quality control research of observational elements in previous studies, such as in Qin et al.
199 (2010).

200 2.2.4 Quality control of Aeolus wind products

201 The quality of the Aeolus HLOS wind products is controlled by validity flags and estimated
202 errors, which are also present in Level 2 B data products. Only data with flags equal to 1 were
203 considered valid. The data were subsequently filtered according to estimated errors, the theoretical
204 values calculated based on the measured signal levels, and the temperature and pressure sensitivity of

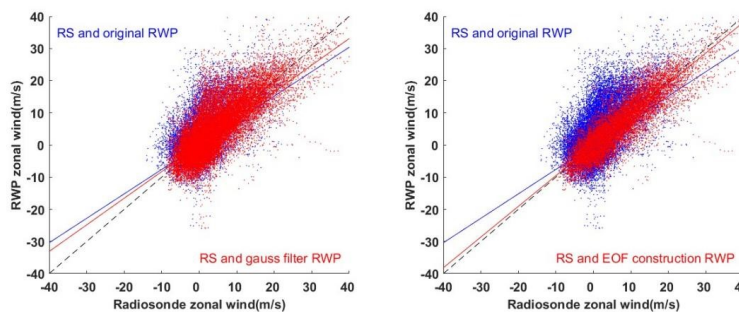


205 the Rayleigh channel response (Dabas et al., 2008). Previous studies have revealed that notable
206 observation errors appeared when the estimated errors were large (Witschas et al., 2020).
207 Consequently, thresholds for estimated errors of 7(5) m/s were applied for Rayleigh(Mie) winds in
208 this study, based on the method described by Guo et al. (2021).

209 3 Results and discussion

210 3.1 Data verification and quality control of WPR

211 Data verification and quality control of the Shapingba WPR were performed based on RS data
212 from the same station. The WPR detects data vertically above the station, while the RS data are
213 derived from air balls, which drift more than 10 kilometers away from the releasing station. Therefore,
214 certain differences exist in the spatial sampling of WPR and RS. Assuming that the atmospheric
215 horizontal distribution is uniform within dozens of kilometers, the WPR and RS wind fields will be
216 comparable. Additionally, the exact release times of the air balls were 23:15 and 11:15 UTC, and they
217 generally took 25 min to rise to 10 km. Therefore, the mean values of the 23:15–00:00 and 11:15–
218 12:00 WPR data were processed to compare the WPR and RS data. Finally, for comparison with the
219 Aeolus data, wind fields derived from WPR and RS data were converted into zonal wind components
220 for data verification and quality control.



221

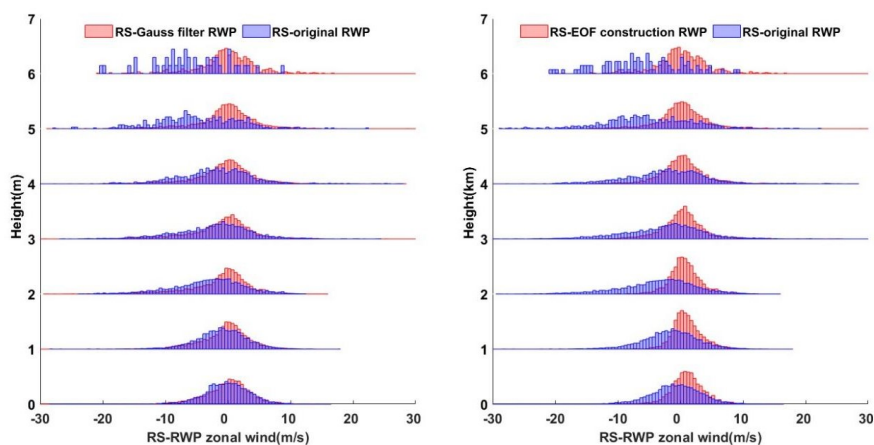
Figure 2: Scatter-plots for (a) original and Gaussian filtering (GF) wind profile data (WPR) vs radiosonde (RS) data, (b) original and empirical orthogonal function construction (EOFc) WPR vs RS data.

222

223 Based on quality control 1 of the WPR data mentioned above, 784 invalid wind speed data were
224 filtered, after which GF and EOFc were conducted on WPR winds. The blue dots in Figure 2
225 represent the scattered distributions of the original WPR and RS data. The correlation coefficient(R)



226 was 69.92%, with scatters distributed along the reference line, indicating a correlation between the
227 two types of data. The number of dots with significant deviation from the reference line between the
228 wind speeds of ± 10 m/s imply large differences between the WPR and RS in the observation of low
229 wind speeds. The red dots in Figure 2(a) are scatter plots of GF-controlled WPR and RS, with an R of
230 76.00%, showing better correlation compared with the original WPR and RS wind data. The GF
231 method screened parts of the data far away from the reference line, which are wind data with large
232 differences between WPR and RS, contributing to an improvement in the correlation of the two types
233 of data. The performance of the WPR data quality control based on EOFc is more significant in
234 Figure 2(b) compared to GF. For EOFc, G is selected to be greater than 85% for the first time;
235 specifically, the first two modes are added after EOF decomposition, with $G = 87.23\%$. The R
236 between the EOFc WPR and RS winds reached 95.44%, with scatters more concentrated around the
237 reference line compared with the original and GF WPR.



238

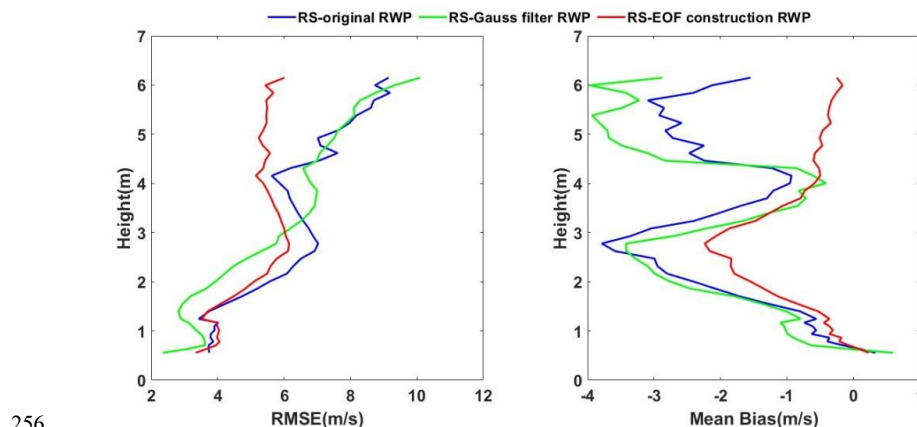
Figure 3: Probability density distributions vertical variations of (a) Radiosonde (RS) minus original and Gaussian filtering (GF) wind profile radar (WPR) data, (b) RS minus empirical orthogonal function construction (EOFc) WPR data.

239

240 The vertical wind deviation distributions of the original and quality-controlled WPR are shown
241 in Figure 3, and the vertical distributions of the statistical parameters are shown in Figure 4. The
242 distribution of deviations between the RS and original WPR data followed normal distribution on
243 various layers. The median of the distribution was centred around 0 near ground within 2km, and
244 gradually moved towards to the negative values above 2km, indicating significant negative deviations



245 on the upper layers. Large negative deviations emerged on different layers, however, large positive
246 deviations were mainly distributed around 3-5 km, with the maximum around 30 m/s. From the
247 perspective of statistical parameters, the RMSE of RS and the original WPR deviation increased with
248 height overall, but decreased at heights between 3 and 4 km. The vertical MB distribution between the
249 RS and original WPR data presents an M-shaped distribution, with positive MB values near the
250 ground and negative values in the other layers. According to the vertical distribution of the deviation
251 scatter points, the negative deviations are significantly larger than the positive deviations. For a
252 relatively small MB value of approximately 4 km, some of the large positive deviations in Figure 3 at
253 this level balance the negative values. Similarly, large positive and negative deviations appeared at
254 approximately 6 km, forming small MB values at this level. In general, wind speeds increase with
255 height, leading to an increase in the observation deviations of the WPR.



256

Figure 4: Vertical distributions of the root mean squared error (RMSE) and mean bias (MB) for (a) Radiosonde (RS) vs original and Gaussian filtering (GF) wind profile radar (WPR) data, (b) RS vs empirical orthogonal function construction (EOFc) WPR data.

257

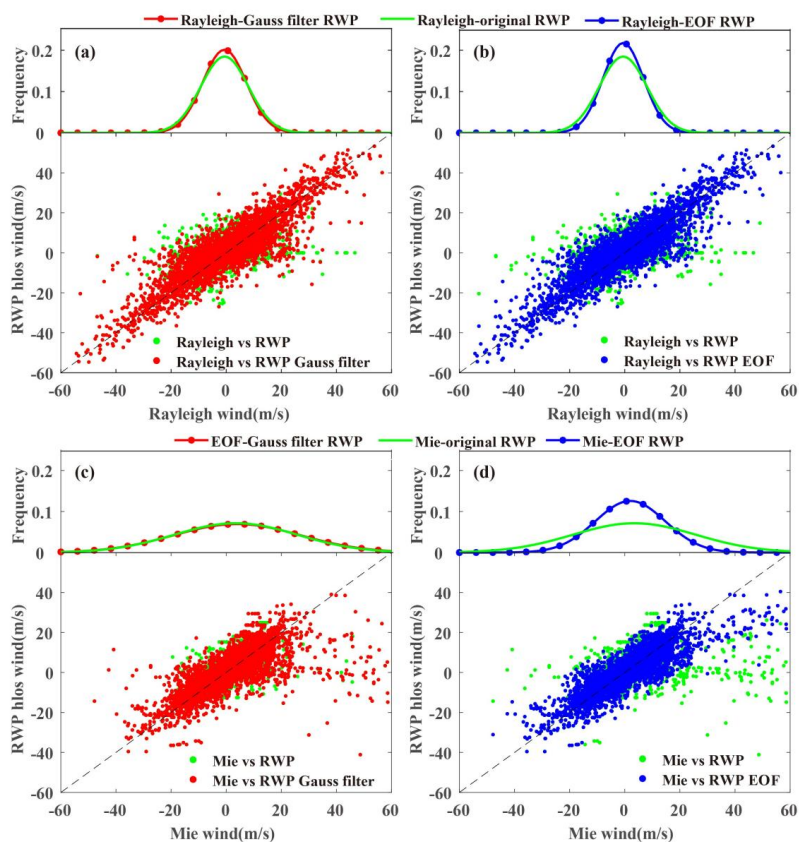
258 Taking RS data as true values, the zonal WPR wind data in Chongqing exhibited various
259 detection errors with height, indicating that quality control of the original WPR data is necessary. The
260 red histograms in Figure 3(a) represent the vertical deviation distributions between RS data and the
261 GF WPR with respect to height. Compared with the original WPR data, GF eliminates some large
262 deviation values of different layers, making the distributions more centred around 0, especially on the
263 upper layers. The vertical distributions of the RMSE and MB between the RS and WPR data
264 correspond to modifications. The RMSE of the RS and GF WPR data is reduced below 3 km



265 compared to the original WPR, while the alteration of MB mainly manifests above 4 km. Remarkably,
266 the negative value of MB above 4 km increased after GF in the WPR data. This was because of the
267 reduction in the larger positive deviation value, and the negative deviation could not be offset.
268 Subsequently, the EOFc method was adopted for the zonal winds in the original WPR data. The
269 vertical deviation distributions of RS and EOFc WPR reduced many large negative deviations in the
270 different vertical layers, making distribuion more in line with normal distribution(Figure 3b). The
271 statistical parameters of the vertical distribution also showed significant changes compared to the
272 original data. A significant decrease in the RMSE value and a notable reduction in the negative MB
273 above 1 km were observed between the RS and EOFc WPR (Figure 4). Combining both the vertical
274 distribution for deviation scatters and statistical parameters, the EOFc WPR winds were similar to the
275 RS data at various heights. Although the deviations of the two types of data were significantly
276 reduced, it is worth noting that the EOFc WPR data have modified the characteristics of the original
277 wind fields to a large extent, especially under strong convective weather conditions with large vertical
278 wind shear. In comparison, the GF WPR data could better retain the basic characteristics of the
279 original wind fields. However, the GF method exhibited a limited reduction in the detection
280 deviations of the WPR data. In general, the two quality control methods have different effects on the
281 reduction of detection deviations and the retention of the original information.



282 3.2 Comparison of the Aeolus and WPR wind data



283

Figure 5: Probability density distributions of deviations and scatter-plots between (a) Rayleigh-clear and (c) Mie-cloudy vs WPR original and Gaussian filtering (GF) WPR winds, (b) Rayleigh-clear and (d) Mie-cloudy vs original and empirical orthogonal function construction (EOFc) WPR winds.

284

285

Owing to the limited spatial coverage of ground-based wind profile data, data verification of Aeolus products in Chongqing was conducted to compensate for the spatial coverage of wind observations to some extent. The obtained results indicate that the Youyang WPR data can be used to verify the Aeolus products described in Section 2. The probability density distribution (PDD) and scatter plots of both Aeolus Rayleigh-clear and Mie-cloudy products versus WPR data are shown in Figure 5. The PDD of deviations between Rayleigh-clear and WPR in Figure 5(a) generally present as a Gaussian distribution, with 82.9% of deviations concentrated between ± 10 m/s and 56.0% of deviations between ± 5 m/s. Quality control with the GF and EOFc methods was conducted on

289

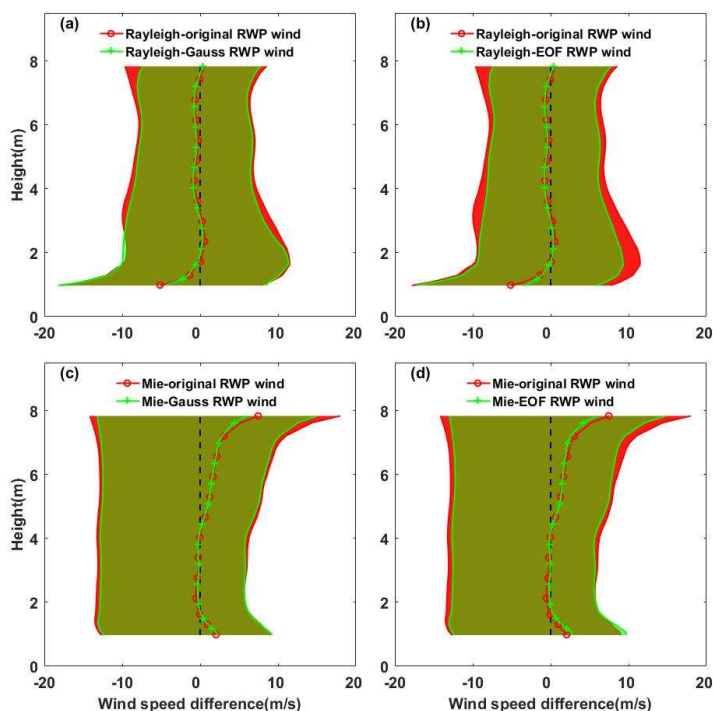
290

291

292



293 original WPR observations, and the PDD of deviations between Rayleigh-clear and quality-controlled
294 WPR winds were concentrated around 0. For deviations between Rayleigh-clear and GF WPR winds,
295 85.8% of deviations were centralized between ± 10 m/s and 58.9% of deviations between ± 5 m/s.
296 In comparison, 86.3% of deviations of Rayleigh-clear and EOFc WPR winds appeared between ± 10
297 m/s and 59.6% of deviations between ± 5 m/s. The scatter distributions of the Rayleigh-clear and
298 WPR winds are shown in Figure 5(a) and 5(b), respectively. A good correlation between
299 Rayleigh-clear and original WPR data was observed, except for some dots far from the reference line,
300 which were scattered with large deviations between the Aeolus and WPR data. Better correlations
301 were observed between the Rayleigh-clear and quality-controlled WPR winds with more scatter
302 centralized around the reference line. Figure 5(c)–(d) show the PDD distribution and scatter plots of
303 the deviations between the Mie-cloudy and WPR winds. We found that 86.2% of deviations of
304 Mie-cloudy versus original WPR data were centralized between ± 10 m/s and 67.8% of deviations
305 between ± 5 m/s, while 86.9% of deviations of Mie-cloudy versus GF WPR winds were centralized
306 between ± 10 m/s and 69.1% of deviations between ± 5 m/s. For the EOFc WPR winds, 87.5% of
307 deviations appeared between ± 10 m/s and 70.2% of deviations between ± 5 m/s. First, the deviations
308 of the Mie-cloudy and quality-controlled WPR data were more concentrated around 0 compared with
309 the original RWP. Most of the scatter points between the Mie-cloudy and original RWP winds were
310 centralized near the reference line. However, a number of dots were concentrated around ± 20 m/s
311 for the WPR winds, and much larger values for the Aeolus data appeared away from the reference
312 line. Additionally, compared with Rayleigh-clear winds, deviations in the Mie-cloudy versus WPR
313 data were small, which may be attributed to the detection principles of the two channels. Compared
314 with the Rayleigh channel, the tracers for the Mie channel, including aerosols and cloud droplets
315 within the boundary layer and in the cloud, mainly centralized at lower vertical levels with smaller
316 wind speeds, resulting in smaller wind deviations for the Mie-cloudy observations.



317

Figure 6: Vertical distribution of mean differences and deviations between (a) Rayleigh-clear vs original and Gaussian filtering (GF) wind profile radar (WPR) data, (b) Rayleigh-clear vs original and empirical orthogonal function construction (EOFc) WPR data, (c) Mie-cloudy vs original and GF WPR data and (d) Mie-cloudy vs original and EOFc WPR data.

318

319 Figure 6 shows the vertical distribution characteristics of the differences between Aeolus
320 products and RWP data. The red solid line represents the vertical distributions of the mean differences
321 between Aeolus and the original RWP data, and the shaded areas denote positive and negative
322 deviations from the mean differences. Mean differences between the Rayleigh-clear and original
323 WPR winds have large negative deviations below 1.5 km, with the maximum deviation reaching
324 -5.2 - 13.0 , -5.2 + 12.61 m/s. However, at a height of 1 km, the mean difference between these data was
325 maintained within ± 1 m/s, with simultaneous decreasing negative and positive deviations with
326 height. The wind measurement capability of the Rayleigh channel is largely limited by the receiving
327 intensity, and the Sichuan Basin is one of the large-value aerosol regions in China (Zhang et al., 2012;
328 Lu et al., 2022a). Particularly, below 1.5 km within the boundary layer, strong aerosol scattering will
329 inevitably affect molecular scattered signals, thus reducing the accuracy of Rayleigh channel wind



330 field inversion (Tan et al., 2017; Guo et al., 2021). In contrast, the vertical distribution of mean
331 differences between Mie-cloudy and original RWP data (Figure 6c and d) showed large values within
332 the boundary layer (below 1.5 km) and middle troposphere (4–8 km). The maximal deviation within
333 the boundary layer reached 2.09–18.23, 2.09+14.76 m/s, while the maximal values were 7.49–19.98,
334 7.49+21.64 m/s in the middle troposphere. For the Mie channel, aerosols and cloud droplet particles
335 were used as tracers for wind measurements. Owing to the influence of the topography in Chongqing,
336 the prevailing quiet and small winds within the boundary layer result in the dominant influence of
337 turbulent motion on large particles (Lu et al., 2022b). This contributes to larger deviations in Mie
338 wind observations because of the irregularity of turbulence. The notable mean differences in the
339 middle troposphere may be affected by the distribution of cloud droplets. Previous studies have
340 revealed that due to the influence of the topography of the Tibetan Plateau, the liquid cloud water
341 contents around 27°N to 35°N in central China are remarkably larger than those in the southern and
342 northern regions at the same altitude (Yang et al., 2012), with nimbostratus and altostratus prevailing
343 in the affected areas (Yu et al., 2004). These may contribute to large mean differences and deviations
344 between Mie winds and WPR data at altitudes of 4–8 km in Chongqing, which is located on the
345 eastern side of the Tibetan Plateau. According to existing observations, the frequency of cloud
346 occurrence in the middle troposphere in spring, autumn, and winter is higher than that in summer,
347 which can explain to some extent why the annual mean differences between Mie winds and RWP
348 around 4–8 km have large values, whereas the average values in summer do not (Guo et al., 2021).
349 Based on the GF and EOFc quality control of the WPR data, the mean differences between the
350 Rayleigh-clear and WPR winds were found to not change significantly, with only some reduction in
351 the differences between the Rayleigh-clear and EOFc WPR data within the boundary layer. However,
352 by controlling the WPR data quality, the positive and negative deviations of the mean difference at
353 various heights can be effectively reduced (Figure 6a and 6b). Specifically, GF can reduce deviations
354 above 3 km, whereas EOFc modifies the positive deviations within the boundary layer. For the Mie
355 winds, a remarkable reduction was observed for mean differences at an altitude of approximately 6–8
356 km and deviations in various layers with quality-controlled WPR data compared with the original
357 WPR data.



358 4 Conclusions

359 To evaluate the observation quality of the multi-source wind profile data in Chongqing, this
360 study matched the Aeolus, RS, and WPR data for 2021. The matching results indicate that the
361 Youyang WPR can be used for comparison with the Aeolus winds. Additionally, data verification and
362 quality control studies of ground-based WPR data were conducted based on Shapingba RS wind
363 observations. The main conclusions are as follows:

364 A correlation was found between the RS and original WPR zonal wind data, with an R of
365 69.92% and scatter points generally distributed along the reference line. The RMSEs of the RS and
366 WPR data increased with height overall, except at an increase of approximately 3–4 km. The MB was
367 vertically distributed in an M-shape, with relatively smaller MB values appearing at 4 and 6 km
368 because of the cancellation of positive and negative deviations.

369 Following screened by the extreme wind climate values and the vertical consistency test, 784
370 WPR wind observations were eliminated. The R between RS versus GF WPR data and EOFc ($G =$
371 87.23) WPR data were 76.00% and 95.44%, respectively, demonstrating a better correlation between
372 RS and EOFc WPR data. A comparison of the deviations in the vertical distribution of the RS and
373 WPR data before and after quality control revealed that the EOFc WPR data are closer to RS winds at
374 various heights, resulting in smaller deviations between the two. However, it should be noted that the
375 EOFc WPR winds have a broader filter than the original data, which can remarkably alter the
376 characteristics of the original wind fields, particularly in cases of severe convection weather
377 conditions where there are significant vertical wind shears. While preserving the basic features of the
378 original wind field, the GF method has a limited impact on reducing the deviations of the original
379 WPR wind observations.

380 The Rayleigh and Mie winds detected by Aeolus exhibited various deviations from the WPR
381 data; 56.0% of deviations between Rayleigh-clear and WPR data existed within ± 5 m/s, while
382 67.8% of deviations existed between Mie-cloudy and 67.8% of deviations between WPR data were
383 within ± 5 m/s. The Mie channel detects aerosols and cloud droplets as tracers, which are lower than
384 the height layers detected by the Rayleigh channel, resulting in relatively small wind speed deviations.
385 However, the mean differences between Rayleigh-clear and WPR winds are smaller than those of
386 Mie-cloudy winds, especially in the middle troposphere of 4–8 km. This may be due to the influence



387 of the topography of the Tibetan Plateau, resulting in a remarkable increase in the liquid cloud water
388 content from 27°N to 35°N in central China compared to other regions. Chongqing is located in the
389 affected areas; thus, the accuracy of Mie wind observations is influenced by the middle troposphere.

390 The deviations between the Aeolus and WPR data changed to some extent after quality control
391 of the WPR data, both for the Rayleigh-clear and Mie-cloudy winds. The scatter points of the Aeolus
392 and WPR data, which were far away from the reference line, decreased; 58.9% of deviations between
393 the Rayleigh-clear and GF WPR data were centralized between ± 5 m/s, and 59.6% of deviations for
394 EOFc WPR data were within ± 5 m/s. For the Mie channel, 69.1% of deviations were concentrated
395 ± 5 m/s between the satellite and GF WPR data, and 70.2% of deviations existed between the Mie
396 and EOFc WPR data. The mean differences of the Rayleigh channel and WPR data changed little
397 after quality control was conducted using both the GF and EOFc methods on WPR data; however,
398 both positive and negative deviations to the mean values decreased. For Mie winds, quality control on
399 WPR made distinct modifications to the mean differences between 6–8 km and deviations to the
400 mean values of all layers between Mie-cloudy and WPR data.

401 **Financial support:** This work was supported by the National Natural Science Foundation of China
402 (42205186), the Chongqing Natural Science Foundation (cstc2021jcyj-msxmX1007), the open
403 research fund of Chongqing Meteorological Bureau (KFJJ-201607) and the key technology research
404 and development of Chongqing Meteorological Bureau (YWJSGG-202215; YWJSGG-202303).

405 **Author contributions:** HL performed data analyses and wrote the initial draft manuscript; MX helped
406 perform the analysis with constructive discussions, reviewed and edited the manuscript, and ensured
407 the accuracy and integrity of the study; HL, MX and WZ acquired financial support for the project
408 leading to this publication; BL conducted the raw data processing and did data correction; WZ, TW
409 and BZ reviewed the manuscript.

410 **Acknowledgments:** We would like to express our gratitude to China Meteorological Bureau to provide
411 the ground-based wind profile data, and the European Space Agency to provide the Aeolus wind
412 products.

413 **Data availability:** The radiosonde and wind profile radar data are available at
414 <http://10.230.90.120:8088/cmadaas/?1689817866009>. The Aeolus satellite data can be downloaded
415 from <https://aeolus-ds.eo.esa.int/oads/access/>.

416 **Conflicts of Interest:** The authors declare no conflict of interest.



417 **Reference**

- 418 Baker W. 2008. Doppler wind lidar: current activities and future plans//Winter T-PARC Workshop.
419 [s.l.]: NOAA/NASA/DoD Joint Center for Satellite Data Assimilation.
- 420 Baker, W. E., Emmitt, G. D., Robertson, F. R., Atlas, R., Molinari, J. E., Bowdle, D. A., Paegle, J. N.,
421 Hardesty, R. M., Menzies, R. T., Krishnamurti, T. N., Brown, R. A., Post, M. J., Anderson, J.
422 R., Lorenc, A. C., and McElroy, J. L. 1995. Lidar-measured winds from space: A key
423 component for weather and climate prediction, *Bulletin of the American Meteorological*
424 *Society* 76, 869-888.
- 425 Barre H M J P, Duesmann B and Kerr Y H. 2008. SMOS: the mission and the system. *IEEE*
426 *Transactions on Geoscience and Remote Sensing*, 46(3): 587-593.
- 427 Belmonte Rivas, M., and Stoffelen, A. 2019. Characterizing ERA-Interim and ERA5 surface wind
428 biases using ASCAT, *Ocean Sci.* 15, 831-852.
- 429 Benjamin, S. G., Schwartz, B. E., Szoke, E. J., and Koch, S. E. 2004. The Value of Wind Profiler Data
430 in U.S. Weather Forecasting, *Bulletin of the American Meteorological Society* 85,
431 1871-1886.
- 432 Beranek R G, Bilbro J W, Fitzjarrald D E, Jones W D, Keller V W and Perrine B S. 1989. Laser
433 atmospheric wind sounder (LAWS)//*Proceedings of SPIE 1062, Laser Applications in*
434 *Meteorology and Earth and Atmospheric Remote Sensing*. Los Angeles: SPIE: 234-248.
- 435 Chen, C., Xue, X., Sun, D., Zhao, R., Han, Y., Chen, T., et al. 2022. Comparison of lower stratosphere
436 wind observations from the USTC's Rayleigh Doppler lidar and the ESA's satellite mission
437 Aeolus. *Earth and Space Science*, 9, e2021EA002176.
- 438 Chen, Z.-Y., Chu, Y.-H., and Su, C.-L. 2021. Intercomparisons of Tropospheric Wind Velocities
439 Measured by Multi-Frequency Wind Profilers and Rawinsonde, *Atmosphere* 12, 1284.
- 440 Dabas, A., Denneulin, M. L., Flamant, P., Loth, C., Garnier, A., and Dolfifi-Bouteyre, A.: Correcting
441 winds measured with a Rayleigh Doppler lidar from pressure and temperature effects, *Tellus*
442 *A*, 60, 206–21.
- 443 Endlich R M, Wolf D E, Hall D J and Brain A E. 1971. Use of a pattern recognition technique for
444 determining cloud motions from sequences of satellite photographs. *Journal of Applied*
445 *Meteorology*, 10(1): 105-117.
- 446 European Space Agency (ESA): “ADM-Aeolus Science Report,” 2008. ESA SP-1311, 121 p.,
447 http://esamultimedia.esa.int/docs/SP-1311_ADM-Aeolus_FINAL_low-res.pdf,
- 448 Gaiser P W, St Germain K M, Twarog E M, Poe G A, Purdy W, Richardson D, Grossman W, Jones W
449 L, Spencer D, Golba G, Cleveland J, Choy L, Bevilacqua R M and Chang P S. 2004. The
450 WindSat spaceborne polarimetric microwave radiometer: sensor description and early orbit
451 performance. *IEEE Transactions on Geoscience and Remote Sensing*, 42(11): 2347-2361.
- 452 Guo, J., Liu, B., Gong, W., Shi, L., Zhang, Y., Ma, Y., Zhang, J., Chen, T., Bai, K., Stoffelen, A., de
453 Leeuw, G., and Xu, X. 2021. Technical note: First comparison of wind observations from
454 ESA's satellite mission Aeolus and ground-based radar wind profiler network of China,
455 *Atmos. Chem. Phys.* 21, 2945-2958.
- 456 King, G. P., Portabella, M., Lin, W., and Stoffelen, A. 2017. Correlating extremes in wind and stress
457 divergence with extremes in rain over the Tropical Atlantic, *EUMETSAT Ocean and Sea Ice*
458 *SAF Scientific Report OSI_AVS_15_02, Version 1.0, available at:*
459 [http://www.osi-saf.org/?q\\$=\\$_content/correlating-extremeswind-and-stress-divergence-extremes-rain-over-tropical-atlantic](http://www.osi-saf.org/?q$=$_content/correlating-extremeswind-and-stress-divergence-extremes-rain-over-tropical-atlantic)).
- 460



- 461 Lu, H., Xie, M., Liu, B., Liu, X., Feng, J., Yang, F., Zhao, X., You, T., Wu, Z., and Gao, Y. 2022a.
462 Impact of atmospheric thermodynamic structures and aerosol radiation feedback on winter
463 regional persistent heavy particulate pollution in the Sichuan-Chongqing region, China,
464 *Science of The Total Environment* 842, 156575.
- 465 Lu, H., Xie, M., Liu, X., Liu, B., Liu, C., Zhao, X., Du, Q., Wu, Z., Gao, Y., and Xu, L. 2022b.
466 Spatial-temporal characteristics of particulate matters and different formation mechanisms of
467 four typical haze cases in a mountain city, *Atmospheric Environment* 269, 118868.
- 468 Marseille G J, Stoffelen A and Barkmeijer J. 2008. Impact assessment of prospective spaceborne
469 Doppler wind lidar observation scenarios. *Tellus A: Dynamic Meteorology and*
470 *Oceanography*, 60(2): 234-248.
- 471 Michelson, S., and Bao, J.-W. 2008. Sensitivity of Low-Level Winds Simulated by the WRF Model in
472 California's Central Valley to Uncertainties in the Large-Scale Forcing and Soil Initialization,
473 *Journal of Applied Meteorology and Climatology - J APPL METEOROL CLIMATOL* 47,
474 3131-3149.
- 475 Njoku E, Christensen E and Cofield R. 1980. The Seasat scanning multichannel microwave
476 radiometer (SMMR): antenna pattern corrections-Development and implementation. *IEEE*
477 *Journal of Oceanic Engineering*, 5(2): 125-137.
- 478 Reitebuch O, Paffrath U and Leike I. 2006. ATBD: ADM-Aeolus Level 1B Product. European Space
479 Research and Technology Centre.
- 480 Rennie, M. P. 2018. An assessment of the expected quality of Aeolus Level-2B wind products, EPJ
481 Web Conf., 176, 02015, <https://doi.org/10.1051/epjconf/201817602015>,
- 482 Sekuła, P., Bokwa, A., Bartyzel, J., Bochenek, B., Chmura, Ł., Gałkowski, M., and Zimnoch, M. 2021.
483 Measurement report: Effect of wind shear on PM10 concentration vertical structure in the
484 urban boundary layer in a complex terrain, *Atmospheric Chemistry & Physics* 21,
485 12113-12139.
- 486 Simonin, D., Ballard, S., and Li, Z. 2014. Doppler radar radial wind assimilation using an hourly
487 cycling 3D-Var with an 1.5km resolution version of the Met Office Unified Model for
488 Nowcasting, *Quarterly Journal of the Royal Meteorological Society* 140.
- 489 Stettner, D., Velden, C., Rabin, R., Wanzong, S., Daniels, J., and Bresky, W. 2019. Development of
490 enhanced vortex-scale atmospheric motion vectors for hurricane applications, *Remote Sens.*,
491 11, 1981, <https://doi.org/10.3390/rs11171981>.
- 492 Sun, X., Zhou, Y., Zhao, T., Bai, Y., Huo, T., Leng, L., He, H., and Sun, J. 2022. Effect of Vertical
493 Wind Shear on PM2.5 Changes over a Receptor Region in Central China, *Remote Sensing*
494 14, 3333.
- 495 Tan, D., Rennie, M., Andersson, E., Poli, P., Dabas, A., de Kloe, J., Marseille, G.-J., and Stoffelen, A.
496 2017. Aeolus Level-2B Algorithm Theoretical Basis Document, Tech. rep.,
497 AE-TN-ECMWFL2BP- 0023, v. 3.0, 109 pp.
- 498 Weber, B. L., & Wuertz, D. B. 1990. Comparison of Rawinsonde and Wind Profiler Radar
499 Measurements, *Journal of Atmospheric and Oceanic Technology*, 7(1), 157-174.
- 500 Weissmann, M., and Cardinali, C. 2007. Impact of airborne Doppler lidar observations on ECMWF
501 forecasts, *Quarterly Journal of the Royal Meteorological Society* 133, 107-116.
- 502 Wernham D, Ciapponi A, Riede W, Allenspacher P, Era F, D'Ottavi A and Thibault
503 D. 2016. Verification for robustness to laser-induced damage for the Aladin instrument on



- 504 the ADM-Aeolus satellite//Proceedings of SPIE 10014, Laser-Induced Damage in Optical
505 Materials 2016. Boulder: SPIE: 1001408.
- 506 Witschas, B., Lemmerz, C., Geiß, A., Lux, O., Marksteiner, U., Rahm, S., Reitebuch, O., and Weiler,
507 F. 2020. First validation of Aeolus wind observations by airborne Doppler wind lidar
508 measurements, *Atmos. Meas. Tech.* 13, 2381-2396.
- 509 Yang Dasheng, Wang Pucui. 2012. Characteristics of Vertical Distributions of Cloud Water Contents
510 over China during Summer[J]. *Chinese Journal of Atmospheric Sciences*, 36(1): 89-101.
- 511 Yu, R., Wang, B., & Zhou, T. 2004. Climate Effects of the Deep Continental Stratus Clouds Generated
512 by the Tibetan Plateau, *Journal of Climate*, 17(13), 2702-2713.
- 513 Zhang C L, Sun X J, Zhang R W, Zhao S J, Lu W, Liu Y W and Fan Z Q. 2019. Impact of solar
514 background radiation on the accuracy of wind observations of spaceborne Doppler wind
515 lidars based on their orbits and optical parameters. *Optics Express*, 27(12): A936-A952.
- 516 Zhang, W., Guo, J., Miao, Y., Liu, H., Zhang, Y., Li, Z., and Zhai, P. 2016. Planetary boundary layer
517 height from CALIOP compared to radiosonde over China, *Atmos. Chem. Phys.* 16,
518 9951-9963.
- 519 Zhang Xubin, Wan Qilin, Xue Jishan, Ding Weiyu, Li Haorui. 2015. Quality control of wind profile
520 radar data and its application to assimilation[J]. *Acta Meteorologica Sinica*, (1): 159-176.
- 521 Zhang, X., Wang, Y., and Niu, T. 2012. Atmospheric aerosol compositions in China: Spatial/temporal
522 variability, chemical signature, regional haze distribution and comparisons with global
523 aerosols, *Atmos Chem Phys* 8, 26571-26615.
- 524 Zhang, Y., J. Guo, Y. Yang, Y. Wang, and S.H.L. Yim. 2020. Vertical wind shear modulates particulate
525 matter pollutions: A perspective from Radar wind profiler observations in Beijing, China.
526 *Remote Sensing*, 12(3), 546.